coatings

MDPI

Article

The Microstructure and Mechanical Properties of Laser-Cladded CoCrFeNiAl/WC Coatings on H13 Steel

Junbo Zhang *, Bing Du, Fuzhen Sun, Yan Li and Yang Liu

State Key Laboratory of Advanced Forming Technology and Equipment, China Academy of Machinery, Science & Technology, Beijing 100044, China
* Correspondence: jbz3596@163.com

Abstract: Previous studies have focused on the laser cladding of high-entropy alloys (HEAs) on untreated H13 steel, yielding promising results. However, there is limited research on laser cladding HEAs on heat-treated H13 steel, which is more common in the automotive mold industry. In this study, CoCrFeNiAl/WC high-entropy alloy composite coatings were fabricated on heat-treated H13 steel using laser cladding, addressing the gap in applying HEAs on heat-treated tool steels. The influence of the WC content on the phase composition, microstructure, and mechanical properties of the composite coating was investigated. The coating exhibits a dual-layer microstructure consisting of a working layer and a transition layer with different compositions. The results indicate that the CoCrFeNiAl/WC working layer primarily consists of FCC phases. As the WC content increases, metallurgical reactions occur in the working layer, forming $(Fe,Co)_3W_3C$, Co_4W_2C, and Cr_7C_3 carbide precipitates. This significantly enhances the hardness and wear resistance of the coating, with the final hardness being 1.23 times that of the substrate, the wear weight loss being only 0.21 times that of the substrate, and the average friction coefficient being only 0.82 times that of the substrate.

Keywords: laser cladding; gradient coating; microstructure; wear mechanism

Academic Editor: Csaba Balázsi

Received: 20 November 2024
Revised: 29 December 2024
Accepted: 30 December 2024
Published: 6 January 2025

Citation: Zhang, J.; Du, B.; Sun, F.; Li, Y.; Liu, Y. The Microstructure and Mechanical Properties of Laser-Cladded CoCrFeNiAl/WC Coatings on H13 Steel. *Coatings* **2025**, *15*, 52. https://doi.org/10.3390/coatings15010052

1. Introduction

The performance of H13 tool steel in additive manufacturing is influenced by various factors, including heat treatment processes, additive manufacturing methods, and surface treatments [1]. During the additive manufacturing of H13 tool steel, heat treatment has a decisive impact on both its thermal and mechanical properties [2]. Heat treatment can enhance its thermal conductivity and thermal stability while also improving mechanical properties such as strength, hardness, and ductility [3,4]. However, when H13 tool steel is used as hot-work die steel, it is prone to wear, primarily due to a decrease in hardness at elevated temperatures [5], which leads to reduced wear resistance [6]. Therefore, surface hardening through heat treatment is often applied in practical production [7]. Nevertheless, molds that have undergone only heat treatment tend to suffer from localized damage during the production process [8]. Laser cladding, as a common coating preparation method, can effectively bond the substrate with the coating material, making it an important approach to enhance the surface properties of H13 steel [9]. Due to its low dilution rate and short processing time, laser cladding technology is widely applied. In preliminary studies on the laser cladding of the H13 surface, conventional materials have been shown to improve the hardness and wear resistance of the coating to some extent. Furthermore, compared to other processing methods, laser cladding can reduce dilution rates, achieve metallurgical bonding, minimize the risk of workpiece deformation, and extend the service life of H13 steel [10,11].

High-entropy alloys (HEAs) are a new class of alloy materials, consisting of five or more metallic elements that are blended in nearly equal proportions, with the atomic percentage of each element ranging from 5% to 35% [12]. This distinctive multi-elemental composition, along with the highly disordered structure, imparts several remarkable properties to HEAs, such as high strength, high hardness, and excellent wear resistance, corrosion resistance, and stability at elevated temperatures [13]. The performance of HEAs is primarily governed by their high mixing entropy, which encompasses thermodynamic high-entropy effects, structural lattice distortions, slow diffusion kinetics, and the "cocktail" effect [14]. These characteristics suggest that HEAs hold considerable promise for a wide variety of applications in engineering fields. In recent years, research has increasingly focused on the laser cladding of HEAs onto H13 steel. Shu et al. [15] used varying laser powers to apply CoCrBFeNiSi HEA coatings on H13 steel. The results showed that as the amorphous content decreased, the composite coatings developed deeper grooves, exhibited more severe adhesive and oxidative wear, and experienced an increase in the width of wear track cross-sections and weight loss, which, in turn, compromised the wear resistance of the coatings. Cai et al. [16] investigated how heat treatment influenced the phase transformation, microstructure, and mechanical properties of the laser-cladded FeCoCrNiAl alloy. Their findings revealed that the cladding layer exhibited a lower activation energy for phase transformation and a higher proportion of iron, resulting from the dilution of the matrix metal, which aided in the formation of the face-centered cubic (FCC) phase. After heat treatment, a greater amount of the FCC phase was precipitated in the cladding layer. The combination of an optimal FCC fixed phase, fine grain strengthening, and dislocation strengthening improved the mechanical properties of the FeCoCrNiAl HEA.

WC is a hard ceramic material commonly utilized as a reinforcement phase in laser cladding technology, owing to its significant ability to enhance the wear and corrosion resistance of composite coatings, thereby improving their overall performance [17]. Akash et al. [18] synthesized AlFeCuCrCoNi-WCx high-entropy alloy (x = 5, 10, and 15 wt.%) coatings via multi-principal-element laser-assisted cladding. The clad zone is predominantly composed of fine, non-oriented, equiaxed grains located away from the substrate, with columnar grains located near the substrate. Microstructural analysis also revealed that an increase in the WC content leads to the refinement of grain size. Peng et al. [19] prepared CoCrFeNi high-entropy alloy coatings reinforced with WC particles using laser cladding. Their findings showed that the laser-cladded coatings exhibited better retention of WC particles within the substrate and demonstrated improved wear resistance. Furthermore, the distribution and morphology of WC particles within high-entropy alloy coatings play a crucial role in influencing the microstructure and overall performance of the coatings, highlighting an important area of research in surface engineering. While the addition of WC particles can improve the mechanical properties of HEAs [20,21], the underlying mechanisms for this improvement are not yet fully understood.

The objective of this study is to enhance the high-temperature wear resistance of H13 steel, which is vital for extending its service life. To achieve this, we have developed a novel strategy that involves designing coatings with alternating soft and hard phases, addressing an oversight in traditional fabrication methods. These coatings are intended to resist deformation through the hard phase and alleviate stress through the soft phase, thereby effectively preventing crack initiation and propagation. In our experimental approach, we utilized CoCrFeNiAl/WCx (x = 0, 10, 20, 30, and 40 wt.%) as the working coating material, using nickel-based 718 powder as a transition layer to fabricate the coatings on H13 steel surfaces. This design yields coatings with a balanced alternating hardness and softness, free from crack-related metallurgical defects.

2. Materials and Methods

2.1. Coating Preparation

This study utilized heat-treated H13 steel samples measuring 30 mm × 18 mm × 18 mm. The surfaces of the samples were polished using a grinder to remove the oxide layer and then cleaned with an alcohol–acetone solution to eliminate oil and other impurities. The chemical composition of H13 is shown in Table 1. The working coating consisted of a CoCrFeNiAl high-entropy alloy in equimolar ratios. The CoCrFeNiAl powder was mixed with WC at the mass ratios specified in Table 2. The powders were mixed for 24 h. The transition layer was made of Inconel 718 powder. The powder morphology used in the experiment is shown in Figure 1a–d, which also show the microstructure of H13 steel, which is mainly composed of martensite, tempered carbides, and retained austenite.

Table 1. Chemical compositions of laser cladding substrate (wt.%) [22].

Element	C	Si	Mn	Cr	Mo	V	S	P	Fe
Mass ratio	0.32~0.45	0.80~1.20	0.20~0.50	4.75~5.50	1.10~1.75	0.80~1.20	≤0.03	≤0.03	Bal.

Table 2. The mass ratio of CoCrFeNiAl high-entropy alloy and WC powders.

Powders	Mass Ratio of HEA	Mass Ratio of WC
CoCrFeNiAl + 10%WC	90	10
CoCrFeNiAl + 20%WC	80	20
CoCrFeNiAl + 30%WC	70	30
CoCrFeNiAl + 40%WC	60	40

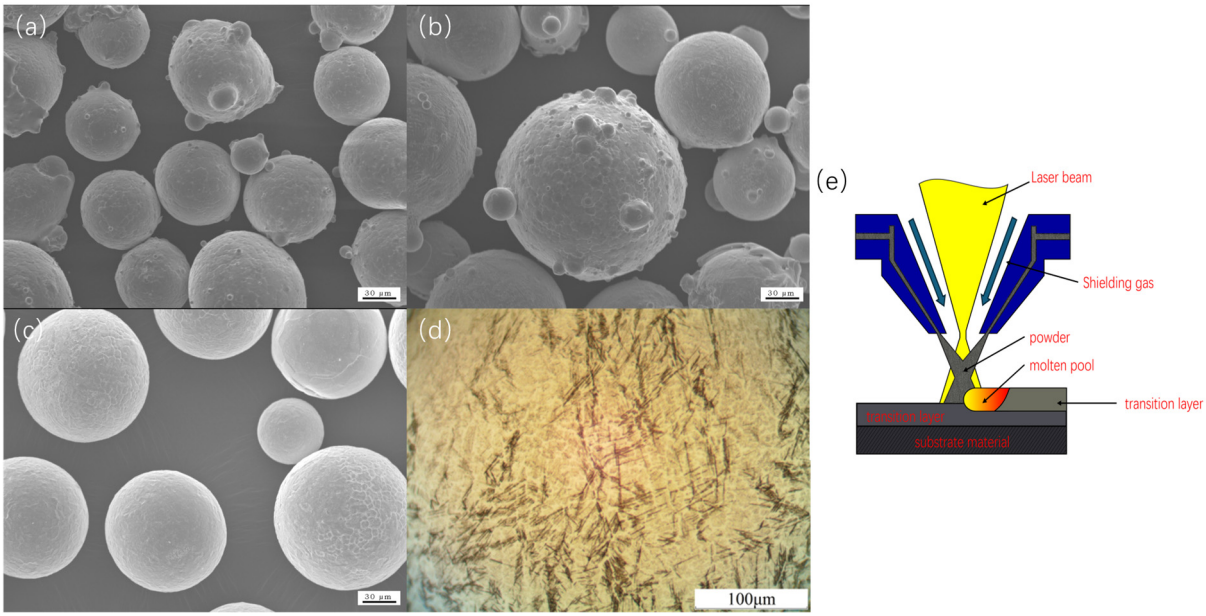

Figure 1. (**a**) AlCoCrFeNi HEA powders; (**b**) Inconel 718 powders; (**c**) spherical WC powders; (**d**) the microstructure of H13 steel; (**e**) process of laser cladding multi-layer composite coating.

The cladding layer was prepared on the surfaces of the H13 samples using laser cladding technology, consisting of a working layer (thickness of 2 mm) and a transition layer (thickness of 1.5 mm). The laser cladding robot used was the LCM6000-2000A high-power laser cladding system developed by the China Academy of Machinery Science and Technology (Beijing, China), featuring an LDF 6000-100 VGP laser head with a laser spot size of 4 mm. The laser power was set to 1.5 kW, with a scanning speed of 6 mm/s and a

powder feed rate of 8.4 g/min for the transition layer. A schematic diagram of the cladding process is shown in Figure 1d. For the working layer, a laser power of 2.4 kW, scanning speed of 12 mm/s, and powder feed rates of 9.6 g/min (0 wt.%), 10.44 g/min (10 wt.%), 11.2 g/min (20 wt.%), 12.03 g/min (30 wt.%), and 12.7 g/min (40 wt.%) were employed. The overlap rate between the working layer and the transition layer was 60%. Argon gas at a flow rate of 11 L/min was used to protect the molten pool from oxidation, with a distance of 20 mm between the laser nozzle and the substrate, utilizing a coaxial powder feeding method.

2.2. Microstructural Characterization and Wear Testing

After the experiment, metallographic samples measuring 10 mm × 10 mm × 10 mm were cut using a wire-cutting machine (Zhongxin, Taizhou, China) and etched with freshly prepared aqua regia for 15 s. The coating structure was observed, and the elemental composition was characterized using a Zeiss scanning electron microscope equipped with an energy-dispersive spectrometer. Hardness testing was conducted using an HVS-1000 Z-type hardness tester (Lidun, Shanghai, China), with a load of 1000 g applied for 14 s. Phase identification was performed using an X-ray diffractometer (D/max-rA) from Rigaku (Tokyo, Japan) under Cu K-α radiation (λ = 1.54 Å, 40 kV, 40 mA). The XRD spectrum was collected in the range of 20° to 110° with a scanning speed of 4°/min. The sample size was 10 mm × 10 mm × 10 mm.

Friction and wear experiments were conducted using an MPX-3G wear testing machine (Hengxu, Jinan, China). GCr15 was chosen as the friction pair, with an external load of 100 N applied for a duration of 30 min at a temperature of 600 °C. Four samples were prepared for each WC concentration and subjected to high-temperature friction and wear tests at 600 °C. Multiple tests were conducted on each sample to ensure the reliability and repeatability of the results. Through these experiments, the effect of varying the WC content on the material's frictional performance and wear behavior was comprehensively assessed.

3. Analysis of Results and Discussion

3.1. Microstructure Composition

Figure 2 illustrates the overall morphology of the coating observed under optical microscopy. The coating surface is free of cracks and porosity, and the interface between the substrate and the transition layer remains intact, without any cracks or pores.

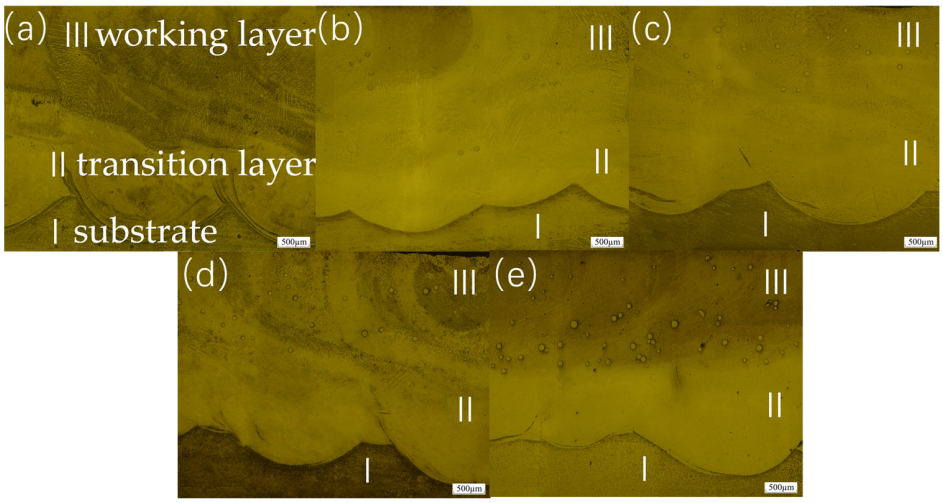

Figure 2. Cross-section topography with different WC additions: (**a**) 0 wt.%; (**b**) 10 wt.%; (**c**) 20 wt.%; (**d**) 30 wt.%; and (**e**) 40 wt.%. The morphology and scale of the microstructure are influenced by the G/R ratio.

Figure 3a shows the X-ray diffraction patterns of CoCrFeNiAl alloys with varying WC weight fractions. When no WC is added, the HEA exhibits a disordered BCC phase, with the strongest characteristic peaks located at 2θ = 44.5°, 65°, 82°, and 98.7°, corresponding to the (110), (200), (211) and (220) crystal planes, respectively [23]. Figure 3b presents an enlarged view of the main diffraction peak of the coating. The figure indicates a distinct shift in the diffraction peak upon the incorporation of WC, suggesting the occurrence of lattice distortion within the coating.

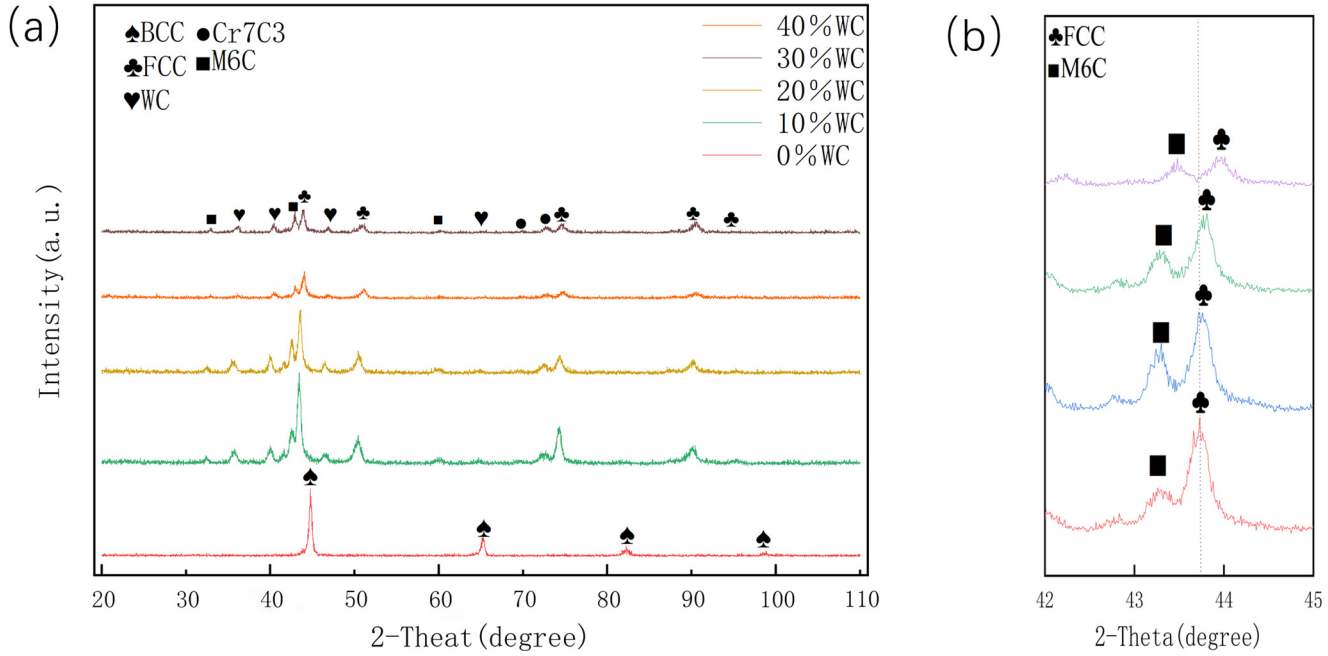

Figure 3. The composite coatings' X-ray diffraction results: (**a**) 20–110° and (**b**) 42–45°.

The main phases of the composite high-entropy alloy coating differ significantly from those of the initial high-entropy alloy coating. This is due to the following reasons: (1) In the composite high-entropy alloy coating, the precipitation of Al is related to the crystal structure of CoCrFeNiAlx and its Al content [23]; as the Al content decreases, the BCC phase transitions into the FCC phase [24,25]. (2) The precipitation of Fe and Cr also promotes the transformation of the disordered BCC phase into the FCC phase. As the WC content increases, the intensity of the FCC phase diffraction peaks gradually decreases, indicating a reduction in the FCC phase content within the composite coating. The strongest characteristic peaks of the FCC phase are located at 2θ = 43.6°, 51.5°, 75°, and 90°, corresponding to the (111), (200), (220), and (311) crystal planes, respectively [23]. Figure 3b presents an enlarged view of the main diffraction peak of the coating. The data indicate a distinct shift in the diffraction peak upon the incorporation of WC, suggesting the occurrence of lattice distortion within the coating. In the composite high-entropy alloy coating, WC reacts metallurgically with CoCrFeNiAl to form Co_4W_2C, Cr_7C_3, $(Fe,Co)_3W_3C$, and $AlNi_3$, with $AlNi_3$ serving as a trace phase of the FCC structure.

Figure 4 presents the EDS line scan results, showing the elemental distribution in the coating. The distribution of elements in the transition coating is observed to be relatively uniform. As illustrated in Figure 5a,b, the 718 alloy demonstrates strong metallurgical bonding between the substrate and the working coating. Figure 5c,d reveal that the transition coating mainly consists of equiaxed and columnar grains, with a layer of planar crystals located in the transition region. Figure 5e highlights the effect of the temperature gradient and solidification rate on the morphology of the microstructure. An excessively high temperature gradient-to-solidification rate ratio (G/R) encourages the formation of

planar crystals. Initially, planar crystals dominate the area near the substrate interface. As crystallization progresses, the temperature gradient (G) decreases, while the solidification rate (R) increases, resulting in a mixed microstructure composed of dendritic and polygonal grains, which align with the heat flow direction. As solidification continues, G continues to decline, while R increases from the base of the molten pool, causing a gradual reduction in the G/R ratio. This reduction destabilizes the planar crystal interface, thereby promoting the growth of a mixed structure of dendritic and polygonal grains along the heat flow direction. As the distance from the bonding interface to the surface of the coating increases, the G/R ratio continues to decrease during solidification. This leads to the development of a hypoeutectic microstructure, with the G/R parameter progressively decreasing from the bottom to the top. In the final stages of solidification, a low G/R ratio facilitates the nucleation and growth of new grains, which expand in all directions and inhibit the growth of columnar dendrites, ultimately forming fine equiaxed grains. Additionally, when a new working layer is applied to the surface of the transition coating, the upper section undergoes remelting and recasting, resulting in the formation of additional fine equiaxed crystals.

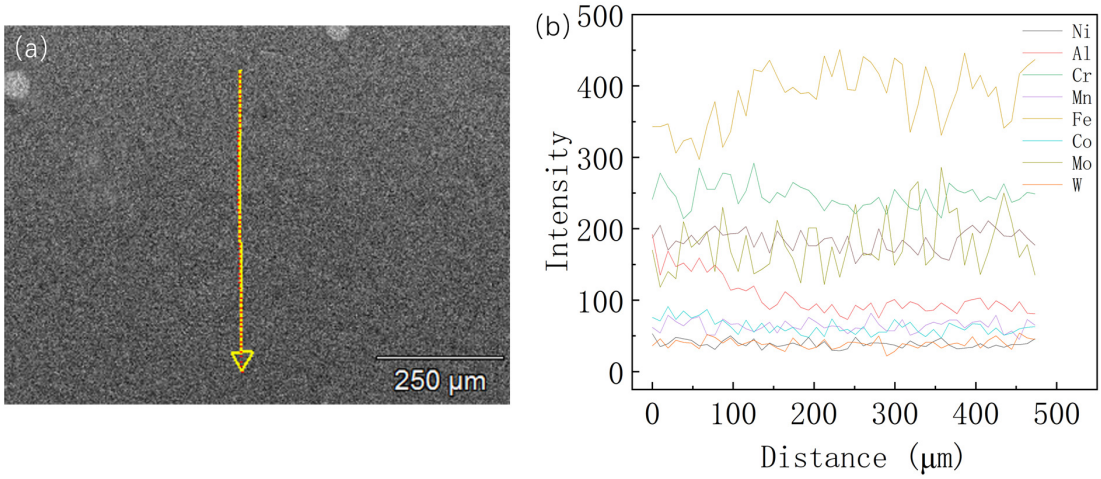

Figure 4. EDS line scan of coatings' microstructure section. (**a**) EDS line scan results; (**b**) Elemental distribution map from the line scan.

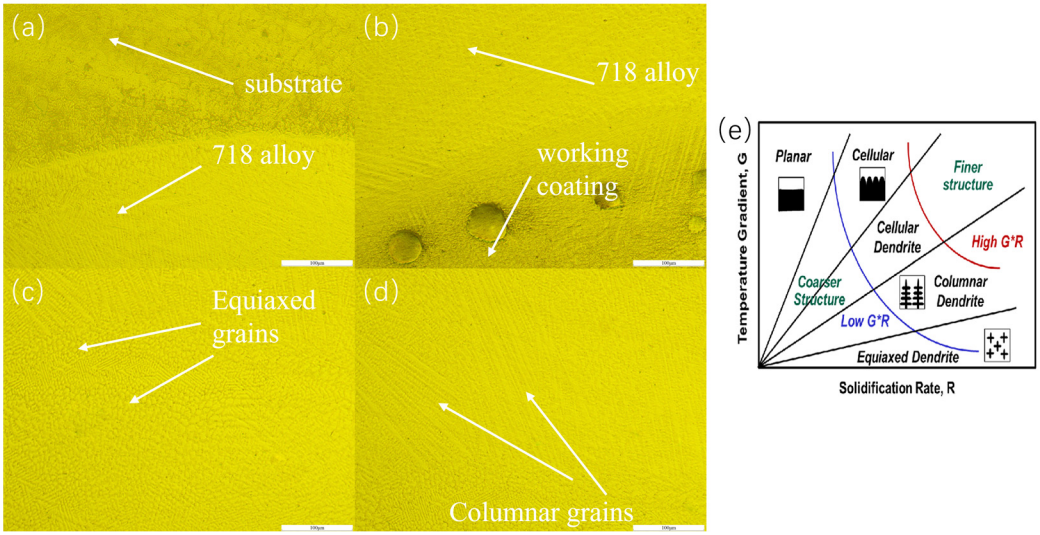

Figure 5. (**a**) The interface between the 718 alloy and the substrate; (**b**) the interface between the 718 alloy and the working coating; (**c**) equiaxed grains in the center of the 718 alloy; (**d**) columnar grains at the bottom of the 718 alloy; (**e**) the influence of G/R on the morphology and scale of the microstructure.

SEM images of the middle part of CoCrFeNiAl alloy cladding layers with varying WC content are shown in Figure 6. It can be observed that when the WC mass fraction is 0, the structure features a periodic alternation of bright and dark phases, predominantly governed by a spinodal decomposition mechanism throughout the material. After the addition of WC particles, as the WC content increases, the grains in the cladding layer are gradually refined, resulting in strong grain interlocking. Grain refinement, which means a reduction in grain size, leads to an increase in yield strength and significantly enhances the boundary density of the cladding layer. This improvement can also enhance the surface strength while slightly increasing its plasticity. The equiaxed grain structure becomes more prevalent, with the grain morphology transitioning from dendritic to a mix of cellular dendrites and columnar dendrites. This change occurs due to the uneven heat diffusion in the molten pool during the laser cladding of WC-containing coatings, leading to the formation of new nucleation points on the columnar dendrites, which gradually grow into cellular dendrites. As the WC content increases, the elongated columnar dendrites transform into smaller cellular dendrites, indicating that the increase in WC content contributes to the refinement of the grains.

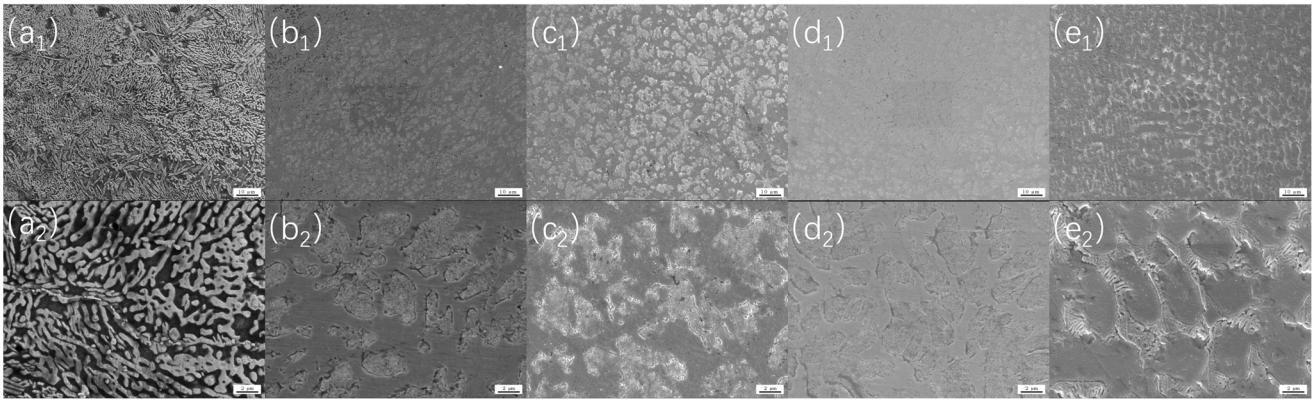

Figure 6. Microstructure of the middle part of CoCrFeNiAl/WC composite coatings (SEM). (**a**–**e**) represent 0~40 wt.% WC, where the subscript 1 corresponds to a magnification of 1000×, and the subscript 2 corresponds to a magnification of 5000×.

Figure 7 illustrates the morphology of WC particles and their surrounding structures in composite coatings with varying WC contents. It can be observed that the WC particles in the coating remain relatively intact, although some surfaces show a few black voids due to laser burning. Additionally, significant amounts of white precipitated phases form around the WC particles, and as the WC content increases, the quantity of these white phases also increases. This indicates metallurgical reactions between WC and CoCrFeNiAl, leading to the formation of gradient interfaces [17]. However, not all WC particles react with CoCrFeNiAl, as shown in Figure 7b. This is because, in this study, higher scanning speeds were used to ensure a uniform distribution of WC in the working layer and to minimize settling phenomena, resulting in reduced rates and extents of in situ reactions due to lower laser heat input.

Figure 8a–d show the morphology of individual WC particles with WC mass fractions ranging from 10% to 40%. Taking a composite coating reinforced with 40% WC as an example, a magnified image of the WC particles and their surrounding morphology can be observed. Figure 8b–d present high-magnification SEM images of the WC particles and their surrounding structures in this coating. From Figure 8, it can be seen that a ring of a gray gradient layer forms around the WC particles, which then expands outward to form a bulk structure. The outer part of the bulk structure consists of a dark high-entropy alloy FCC phase and a fish-like structure. EDS point scanning analysis was conducted at selected

locations, as shown in Figure 8e, where point 1 represents the fish-like structure and point 2 represents the bulk structure; specific data can be found in Table 3. The EDS analysis reveals that both types of structures contain certain proportions of W and C, confirming that they are both precipitation phases of WC particles. However, there are differences in the ratios of W and C among the different precipitation phases. The contents of W and C in the bulk precipitate vary significantly, while in the fish-like precipitate, the content differences are minor. This indicates that, in addition to morphological differences, there are also compositional differences. Specifically, the content of W in the fish-like structure is lower than that in the bulk structure, which may be due to the fact that the bulk structure is formed directly through the diffusion of WC particles, while the fish-like structure results from a eutectic reaction between WC particles and the high-entropy alloy matrix. However, not all WC particles react with CoCrFeNiAl, as shown in Figure 8a. This is because, in this study, higher scanning speeds were used to ensure a uniform distribution of WC in the working layer and to minimize settling phenomena, resulting in reduced rates and extents of in situ reactions due to lower laser heat input.

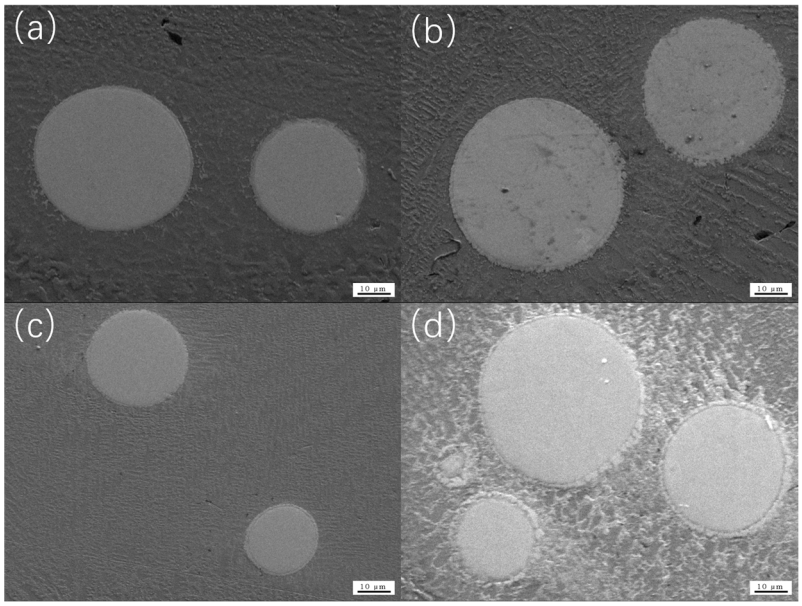

Figure 7. Microstructure of WC particles and their surrounding structures in composite coatings with varying WC contents: (**a**) 10 wt.%; (**b**) 20 wt.%; (**c**) 30 wt.%; and (**d**) 40 wt.%.

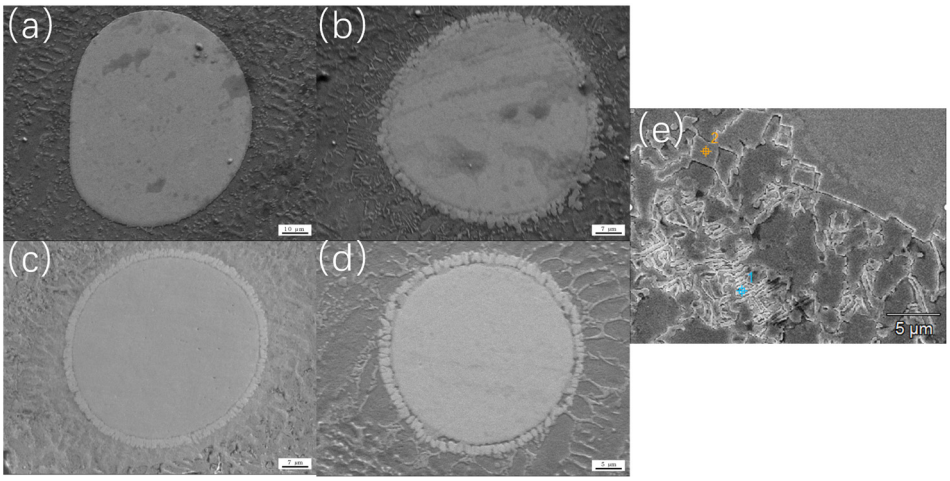

Figure 8. WC particles in WC-reinforced composite coatings with different WC content: (**a**) 10 wt.%; (**b**) 20 wt.%; (**c**) 30 wt.%; and (**d**) 40 wt.%. (**e**) EDS point scanning.

Table 3. The results of point energy spectrum analysis for the cladding layer in different areas (wt.%).

Location	Co	Cr	Fe	Ni	Al	W	C	Nb
1	0.4	12.03	24.99	15.01	1.10	42.13	4.30	0.03
2	0.1	8.3	14.14	6.97	0.03	65.38	3.26	1.81

Using a WC content of 40% as an example, EDS point scan analysis was conducted on the different microstructures, as shown in Figure 9, to investigate the elemental distribution in each region. The scanning results are shown in Table 4. Some regions exhibit a biphasic spinodal decomposition structure, where equiaxed dendrites experience coarsening. The gray regions at the dendrite edges are the A2 phase enriched with Al and Ni alloys. Significant segregation of W and C elements was observed, while Fe and Ni exhibited segregation within the FCC phase, with Cr and Co elements being relatively uniformly distributed. Due to the large atomic size of W, its solubility is limited, leading to its predominant distribution in the inter-dendritic regions. The tendency toward elemental segregation can also be inferred from the enthalpy of mixing values, with smaller values indicating a greater likelihood of element enrichment. Specific values can be found in Table 5. The analysis indicates that the enthalpy of mixing of C and W is the highest, suggesting that C is most likely to be concentrated with W in the inter-dendritic regions. The enrichment of W and C in these areas facilitates metallurgical reactions with Fe, resulting in the formation of M_6C-type carbides; hence, Fe tends to be distributed in the inter-dendritic regions. Due to the higher concentrations of Ni and Cr in the transition coating, their distributions are relatively uniform, where they react with W and C to form compounds such as $(Fe,Co)_3W_3C$, Co_4W_2C, and Cr_7C_3.

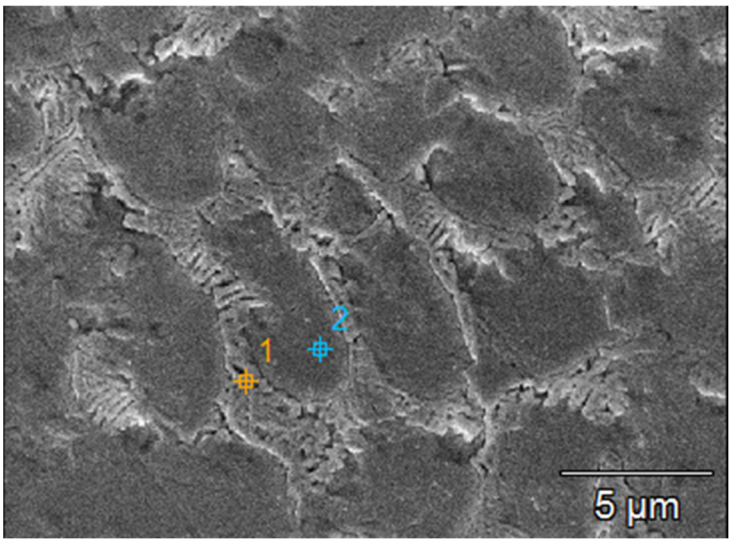

Figure 9. The SEM image of the central region of the working coating. Point 1 is at the grain boundary, and point 2 is inside the grain boundary.

Table 4. Point energy spectrum analysis results of the cladding layer in different areas (wt.%).

Location	Co	Cr	Fe	Ni	Al	W	C	Mo	Nb
1	1.56	13.61	14.49	7.81	0.17	49.61	3.97	4.43	4.34
2	3.29	11.45	35.39	24.98	3.35	18.86	1.78	0.87	0.02

Table 5. Mixing enthalpy between elements [26].

Mixing Enthalpy	Fe	Al	C	Co	Ni	W	Cr
Fe	/						
Al	−11	/					
C	−50	−36	/				
Co	−1	−19	−42	/			
Ni	−2	−22	−39	0	/		
W	0	26	−60	−1	−3	/	
Cr	−1	−10	−61	−4	−7	1	/

3.2. Hardness Analysis

Figure 10 shows the Vickers hardness of CoCrFeNiAl high-entropy alloy composite coatings with varying WC mass fractions. It is evident that as the WC content increases, the hardness of the coating also increases consistently. The average hardness values for the WC00, WC10, WC20, WC30, and WC40 coatings are 508.01 HV, 530.67 HV, 558.34 HV, 589.67 HV, and 617.08 HV, respectively. The hardness exhibits a U-shaped distribution from the working layer to the substrate, with average hardness values of 279.47 HV for the transition layer and 498.71 HV for the substrate. The working layer, transition layer, and substrate together form a sandwich structure of soft and hard combinations.

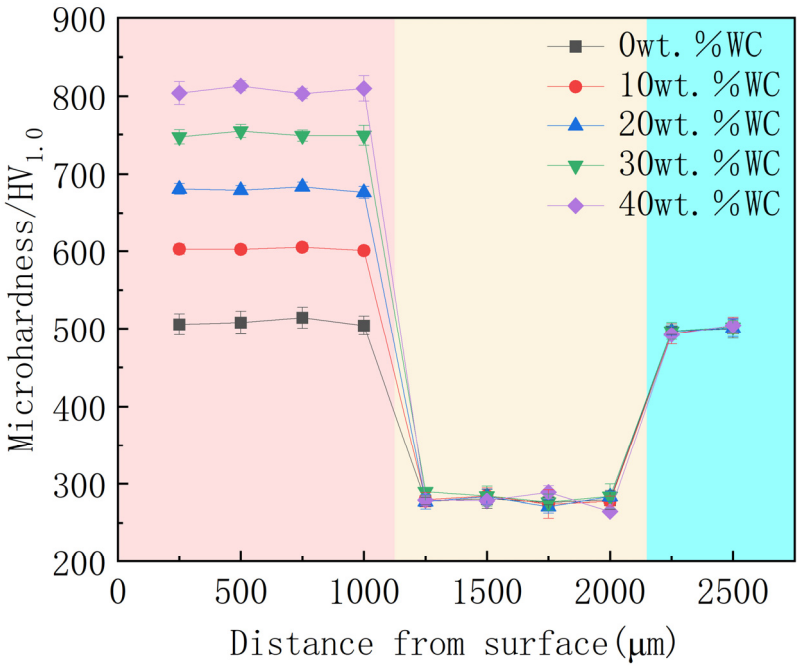

Figure 10. Hardness map of CoCrFeNiAl high-entropy alloy composite coatings with different mass fractions of WC. The color on the left represents the working coating, the color in the middle represents the transition coating, and the color on the right represents the substrate.

Figure 10 shows the hardness contributions from different strengthening mechanisms. The strengthening mechanisms of laser-cladded CoCrFeNiAl/WC composite coatings can be categorized into four main aspects: (1) Solid solution strengthening: during the laser cladding process, some WC particles decompose, allowing W and C atoms to enter the FCC phase, which enhances solid solution strengthening, as shown in Figure 11. (2) Dislocation strengthening: Rapid solidification during laser cladding generates high thermal stresses, leading to a high density of dislocations [27]. The FCC phase, lacking the BCC phase's semi-coherent phase boundaries, facilitates dislocation storage [20]. The incorporation of

W and C atoms into the FCC phase causes lattice distortion, hindering dislocation slip deformation. (3) Precipitation strengthening: the decomposition of WC particles results in metallurgical reactions with CoCrFeNiAl, forming M_6C_3 and Cr_7C_3 precipitates that significantly improve material hardness by obstructing dislocation movement. (4) Grain refinement: the presence of WC particles and newly formed carbides increases the number of heterogeneous nucleation points, leading to grain refinement.

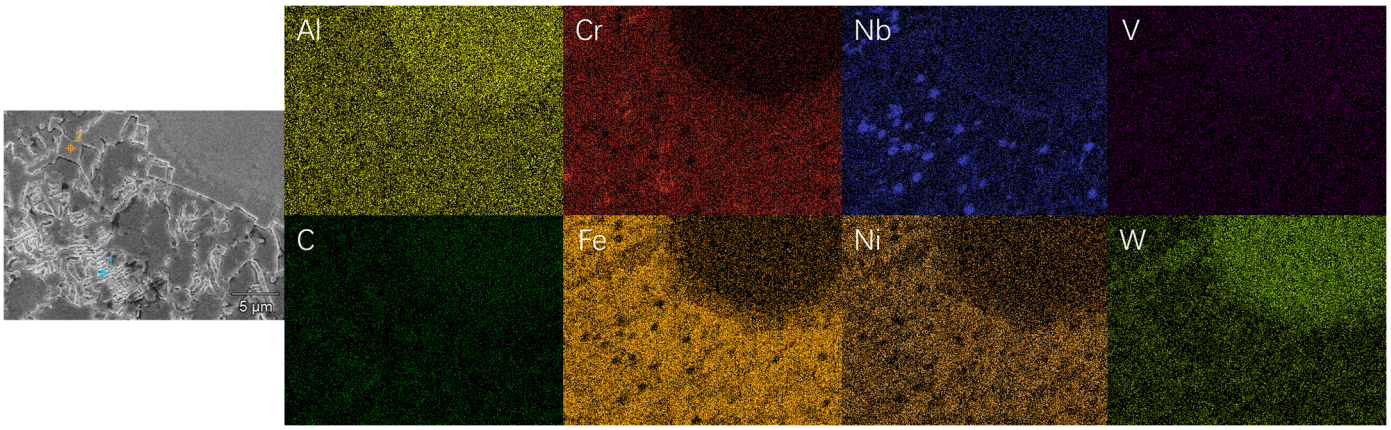

Figure 11. EDS scanning map of different microstructures. Point 1 is blocky structure, and point 2 is fishbone-like structure.

3.3. Wear Behavior

As shown in Figure 12, the weight loss, friction coefficient, and average friction coefficient of CoCrFeNiAl/WC coatings with different WC contents are presented. The friction coefficient curve initially exhibits significant fluctuations, stabilizing after a break-in period. Influenced by grain size and compositional segregation, the friction coefficient curve shows a serrated characteristic. The fluctuation of the friction coefficient in the early stages of wear is attributed to the contact between the micro-convex surface and the grinding ball, where the surface protrusions are cut into abrasive particles during friction, resulting in a "plowing" effect on the specimen's surface. As the friction process continues, the roughness of the sample surface decreases, leading the friction coefficient to enter a stable phase. The average friction coefficients for coatings with different WC contents (wt. = 0%, 10%, 20%, 30%, and 40%) are 0.250, 0.243, 0.234, 0.220, and 0.208, respectively. With the increasing WC content, the wear resistance of the coatings significantly improves, resulting in reduced weight loss, attributed to the combined effects of solid solution strengthening, dislocation strengthening, grain refinement, and precipitation strengthening.

As shown in Figure 13, the microstructural surface morphology of the experimental alloy after friction and wear testing is presented. The high-temperature friction and wear test induces severe plowing effects on the specimens. As shown in Figure 13a–c, with the increasing WC content, the number of deep grooves progressively decreases, while the friction surface maintains a relatively high roughness.However, due to the high-temperature stability of CoCrFeNiAl, no adhesive layer is observed. As shown in Figure 13d,e, the plowing effect is significantly reduced, with the best resistance to plastic deformation achieved at 40% WC content. Throughout the wear process, oxidative wear is consistently present. The dot-like protrusions on the specimens are wear debris fragments.

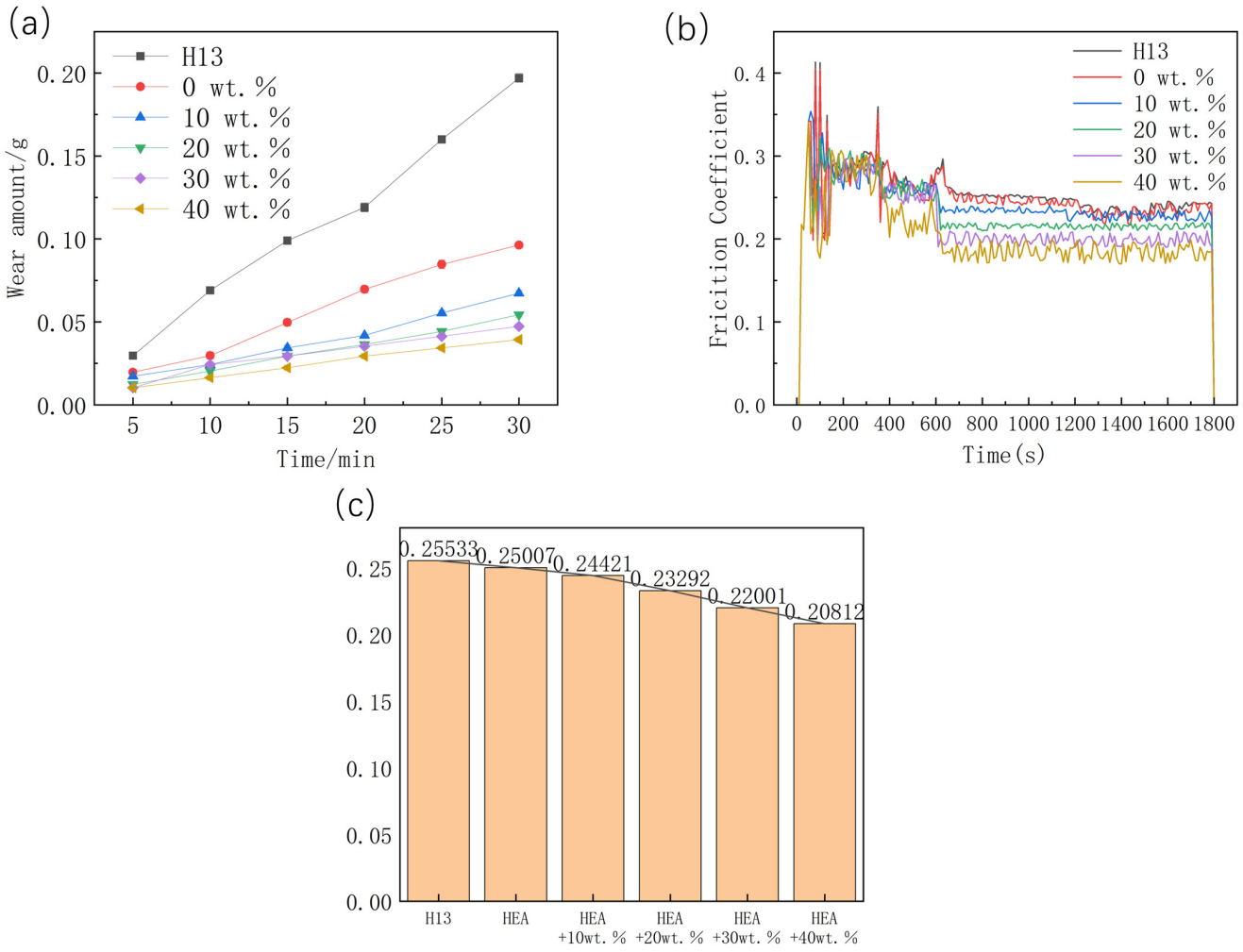

Figure 12. (**a**) Weight loss of CoCrFeNiAl/WC composite coatings; (**b**) friction coefficient; (**c**) average friction coefficient.

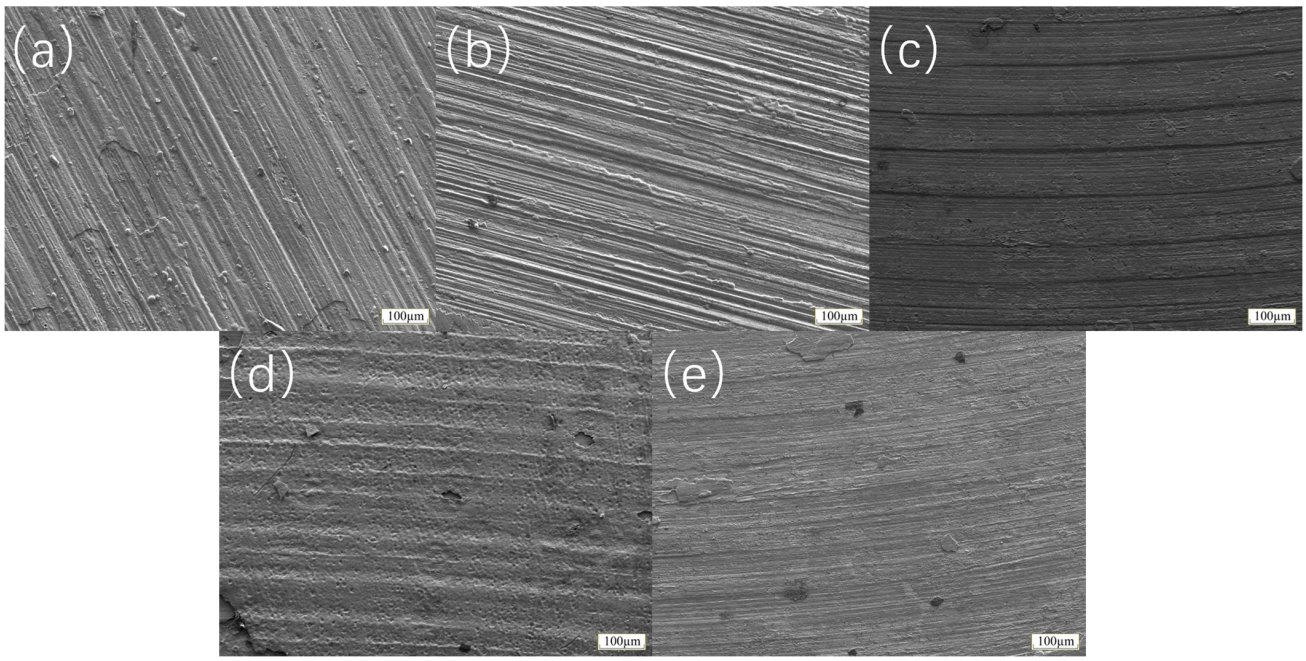

Figure 13. Worn surface morphologies of CoCrFeNiAl/WC composite coatings. (**a**) 0 wt.% WC; (**b**) 10 wt.% WC; (**c**) 20 wt.% WC; (**d**) 30 wt.% WC; and (**e**) 40 wt.% WC.

4. Conclusions

In this study, alternating soft and hard coatings were applied to the surface of an H13 substrate using laser cladding technology to enhance the high-temperature wear resistance of hot-work tool steels. The effects of different WC contents on the phase composition, microstructure, and mechanical properties of the coatings were investigated. The following key conclusions can be drawn:

(1) The laser-cladded CoCrFeNiAl coating predominantly exhibits a body-centered cubic (BCC) phase, whereas the CoCrFeNiAl/WC composite coating shows a transition from the BCC phase to the face-centered cubic (FCC) phase. As the WC content increases, the volume fraction of precipitates (such as $(Fe,Co)_3W_3C$, Co_4W_2C, Cr_7C_3, etc.) gradually increases. When the WC content reaches 40%, the volume fraction of the precipitates is maximized.

(2) An increase in WC content significantly enhances the hardness of the coating. At 40% WC, the coating hardness reaches 617 HV. This hardness improvement can be attributed to the following mechanisms: (a) Solid solution strengthening: W and C atoms enter the FCC phase, causing lattice distortion and producing solid solution strengthening effects. (b) Dislocation strengthening: the high thermal stresses induced during the laser cladding process increase the dislocation density, and the lattice distortion impedes dislocation motion during slip deformation. (c) Precipitation strengthening: W and C atoms react with the CoCrFeNiAl alloy to form precipitates such as M_6C_3 and Cr_7C_3, significantly improving hardness and inhibiting dislocation motion. (d) Grain refinement strengthening: the WC particles and newly formed carbide precipitates provide heterogeneous nucleation sites, promoting grain refinement.

(3) As the WC content increases, the high-temperature wear resistance of the CoCrFeNiAl/WC composite coating becomes significantly improved. At 40% WC, the coating exhibits the best wear resistance, characterized by an average friction coefficient of 0.208 and a mass loss of 0.04 g.

Author Contributions: J.Z., investigation and writing—original draft preparation; B.D., investigation and methodology; F.S., data curation and investigation; Y.L. (Yang Liu), conceptualization and writing—reviewing and editing; Y.L. (Yan Li), conceptualization and writing—reviewing and editing. All authors have read and agreed to the published version of the manuscript.

Funding: The authors would like to express their special thanks for the financial support obtained from the Technology Development Fund Project of China Academy of Machinery Science and Technology Group (2022110032011383) and Hebei Province Central Government-guided Local Science and Technology Special Project Funding (246Z1824G).

Institutional Review Board Statement: Not applicable.

Informed Consent Statement: Not applicable.

Data Availability Statement: Data are contained within the article.

Conflicts of Interest: The authors declare no conflicts of interest.

References

1. Guenther, E.; Kahlert, M.; Vollmer, M.; Niendorf, T.; Greiner, C. Tribological Performance of Additively Manufactured AISI H13 Steel in Different Surface Conditions. *Materials* **2021**, *14*, 928. [CrossRef] [PubMed]
2. Telasang, G.; Dutta Majumdar, J.; Padmanabham, G.; Manna, I. Structure–Property Correlation in Laser Surface Treated AISI H13 Tool Steel for Improved Mechanical Properties. *Mater. Sci. Eng. A* **2014**, *599*, 255–267. [CrossRef]
3. Åsberg, M.; Fredriksson, G.; Hatami, S.; Fredriksson, W.; Krakhmalev, P. Influence of Post Treatment on Microstructure, Porosity and Mechanical Properties of Additive Manufactured H13 Tool Steel. *Mater. Sci. Eng. A* **2019**, *74*, 584–589. [CrossRef]

4. Sun, Y.; Wang, J.; Li, M.; Wang, Y.; Li, C.; Dai, T.; Hao, M.; Ding, H. Thermal and Mechanical Properties of Selective Laser Melted and Heat Treated H13 Hot Work Tool Steel. *Mater. Des.* **2022**, *224*, 111295. [CrossRef]
5. Balaško, T.; Vončina, M.; Medved, J. Simultaneous Thermal Analysis of the High-Temperature Oxidation Behaviour of Three Hot-Work Tool Steels. *J. Therm. Anal. Calorim.* **2023**, *148*, 1251–1264. [CrossRef]
6. Pedroso, S.; Abrão, A.M.; Rodrigues, E.; Câmara, M.A. Surface Modification of AISI H13 Steel by Die-Sinking Electrical Discharge Machining and TiAlN Coating: A Promising Hybrid Technique to Improve Wear Resistance. *Wear* **2020**, *462*, 203509. [CrossRef]
7. Telasang, G.; Dutta Majumdar, J.; Padmanabham, G.; Manna, I. Wear and Corrosion Behavior of Laser Surface Engineered AISI H13 Hot Working Tool Steel. *Surf. Coat. Technol.* **2015**, *261*, 69–78. [CrossRef]
8. Siddiqui, A.A.; Dubey, A.K. Recent Trends in Laser Cladding and Surface Alloying. *Opt. Laser Technol.* **2021**, *134*, 106619. [CrossRef]
9. Pei, Y.T.; Th, J.; De Hosson, M. Functionally Graded Materials Produced by Laser Cladding. *Acta Mater.* **2000**, *48*, 2617–2624. [CrossRef]
10. Lu, J.Z.; Xue, K.N.; Lu, H.F.; Xing, F.; Luo, K.Y. Laser shock wave-induced wear property improvement and formation mechanism of laser cladding Ni25 coating on H13 tool steel. *J. Mater. Process. Technol.* **2021**, *296*, 117202. [CrossRef]
11. Lu, H.F.; Xue, K.N.; Xu, X.; Luo, K.Y.; Xing, F.; Yao, J.H.; Lu, J.Z. Effects of laser shock peening on microstructural evolution and wear property of laser hybrid remanufactured Ni25/Fe104 coating on H13 tool steel. *J. Mater. Process. Technol.* **2021**, *291*, 117016. [CrossRef]
12. Yeh, J.W.; Chen, S.K.; Lin, S.J.; Gan, J.Y.; Chin, T.S.; Shun, T.T.; Tsau, C.H.; Chang, S.Y. Nanostructured High-Entropy Alloys with Multiple Principal Elements: Novel Alloy Design Concepts and Outcomes. *Adv. Eng. Mater.* **2004**, *6*, 299–303. [CrossRef]
13. Ding, Q.; Fu, X.; Chen, S.; Bei, H.; Li, J.; Zhang, Z.; Yu, Q.; Zhang, Y.; Chen, D.; Wen, M.; et al. Tuning Element Distribution, Structure and Properties by Composition in High-Entropy Alloys. *Nature* **2019**, *574*, 223–227. [CrossRef] [PubMed]
14. Rogachev, A.S. Structure, Stability, and Properties of High-Entropy Alloys. *Phys. Met. Metallogr.* **2020**, *121*, 733–764. [CrossRef]
15. Shu, F.Y.; Zhang, B.L.; Liu, T.; Sui, S.H.; Liu, Y.X.; He, P.; Liu, B.; Xu, B.S. Effects of Laser Power on Microstructure and Properties of Laser Cladded CoCrBFeNiSi High-Entropy Alloy Amorphous Coatings. *Surf. Coat. Technol.* **2019**, *358*, 667–675. [CrossRef]
16. Cai, Y.; Shan, M.; Manladan, S.M.; Zhu, L.; Gao, F.; Sun, D.; Han, J. Effect of High Temperature Heat Treatment on Microstructure and Properties of FeCoCrNiAl High-Entropy Alloy Laser Cladding Layer. *Mater. Charact.* **2022**, *191*, 112137. [CrossRef]
17. Rong, T.; Gu, D.D.; Shi, Q.M.; Cao, S.N.; Xia, M.J. Effects of Tailored Gradient Interface on Wear Properties of WC/Inconel 718 Composites Using Selective Laser Melting. *Surf. Coat. Technol.* **2016**, *307*, 418–427. [CrossRef]
18. Vyas, A.; Menghani, J.; Natu, H. Influence of WC Particle on the Metallurgical, Mechanical, and Corrosion Behavior of AlFeCuCrCoNi-WC_x High-Entropy Alloy Coatings. *J. Mater. Eng. Perform.* **2021**, *30*, 2449–2461. [CrossRef]
19. Peng, Y.B.; Zhang, W.; Li, T.C.; Zhang, M.Y.; Wang, L.; Song, Y.; Hu, S.H.; Hu, Y. Microstructures and Mechanical Properties of FeCoCrNi High Entropy Alloy/WC Reinforcing Particles Composite Coatings Prepared by Laser Cladding and Plasma Cladding. *Int. J. Refract. Met. Hard Mater.* **2019**, *84*, 105044. [CrossRef]
20. Li, X.F.; Feng, Y.H.; Liu, B.; Yi, D.H.; Yang, X.H.; Zhang, W.D.; Chen, G.; Liu, Y.; Bai, P.K. Influence of NbC Particles on Microstructure and Mechanical Properties of AlCoCrFeNi High-Entropy Alloy Coatings Prepared by Laser Cladding. *J. Alloys Compd.* **2019**, *788*, 485–494. [CrossRef]
21. Peng, Y.; Zhang, W.; Li, T.; Zhang, M.; Wang, L.; Hu, S. Microstructures and wear-resistance of WC-reinforced high entropy alloy composite coatings by plasma cladding: Effect of WC morphology. *Surf. Eng.* **2021**, *37*, 678–687. [CrossRef]
22. Gao, Y.; Jiang, S.; Bai, S.; Jie, M.; Zhang, D.; Liu, Y. Microstructure and Mechanical Properties of FeCoCrNiAl + WC Composite Coating Formed by Laser Cladding on H13. *Coatings* **2024**, *14*, 1259. [CrossRef]
23. Zhou, P.L.; Xiao, D.H.; Zhou, P.F.; Yuan, T.C. Microstructure and Properties of Ultrafine Grained AlCrFeCoNi/WC Cemented Carbides. *Ceram. Int.* **2018**, *44*, 17160–17166. [CrossRef]
24. Hui, J.; Qin, J.; Zhou, Y.; Sun, X.; Dong, W.; Zhu, S. Effect of Al Content in CoCrFeNiAlx HEA on Mechanical Properties and High Temperature Oxidation Resistance of WC-10%CoCrFeNiAlx Hard Alloy. *Int. J. Refract. Met. Hard Mater.* **2024**, *122*, 106712. [CrossRef]
25. Dong, W. Effect of Phase Transformation of CoCrFeNiAl High-Entropy Alloy on Mechanical Properties of WC-CoCrFeNiAl Composites. *Ceram. Int.* **2023**, *49*, 32388–32398. [CrossRef]
26. Xu, L.; Li, M.; Song, Z.; Li, F.; Guo, J.; Gao, M. WC-High Entropy Alloy Reinforced Long Life Self-Grinding Silage Knife Prepared by Laser Cladding. *Nanomaterials* **2022**, *12*, 1013. [CrossRef]
27. Wang, Q.N.; Lu, Y.P.; Yu, Q.; Zhang, Z. The Exceptional Strong Face-centered Cubic Phase and Semi-coherent Phase Boundary in a Eutectic Dual-phase High Entropy Alloy AlCoCrFeNi. *Sci. Rep.* **2018**, *8*, 14910. [CrossRef]